

Short Communication

Fatigue performance of U-notched additively manufactured AlSi10Mg parts: The effects of chemical and thermal post-treatments

Erfan Maleki^{a,b,*}, Sara Bagherifard^c, Nabeel Ahmad^{a,b}, Shuai Shao^{a,b}, Okan Unal^{d,e}, Mario Guagliano^c, Nima Shamsaei^{a,b}

^a National Center for Additive Manufacturing Excellence (NCAME), Auburn University, Auburn, AL 36849, United States

^b Department of Mechanical Engineering, Auburn University, Auburn, AL 36849, United States

^c Department of Mechanical Engineering, Politecnico di Milano, Milano 20158, Italy

^d Department of Mechanical Engineering, Karabuk University, Karabuk 78050, Turkey

^e Modern Surface Engineering Laboratory (MSELAB), Karabuk University, Karabuk 78050, Turkey

ARTICLE INFO

Keywords:

Additive manufacturing (AM)
AlSi10Mg
Electro-chemical polishing (ECP)
Finite element analysis, Notch
Fatigue

ABSTRACT

In the current study, the effects of different post-processing methods, including heat treatment (HT) and electro-chemical polishing (ECP) as well as their combination on the surface texture, porosity, microstructure, mechanical properties, and rotating bending fatigue behavior of U-notched laser powder bed fused AlSi10Mg specimens were comprehensively investigated. In addition, to better understand the effects of the applied post-processing methods on the sensitivity of the notched specimen to surface and near-surface defects, finite element analysis was performed. Chemical treatment was found to be very influential on surface texture modification of the very narrow notched parts, for which the application of other treatments can be quite challenging. It was also found that the fatigue behavior of the notched specimens was more sensitive to the surface texture rather than to the near-surface defects. The hybrid treatment involving HT+ECP was the most effective for fatigue behavior improvement due to simultaneous homogenization of the microstructure, released tensile residual stresses, enhanced ductility and high surface texture modification.

1. Introduction

Laser powder bed fusion (L-PBF), as one of the popular additive manufacturing (AM) techniques, can fabricate metallic parts with intricate geometries and decent dimensional accuracies. However, as-built manufactured parts by L-PBF often contain different types of surface and internal anomalies due to the complex melting and solidification phenomena and rapid cooling [1,2]. The stress concentrations induced by surface anomalies can accelerate fatigue crack initiation and fatigue failure [3–5]. Consequently, applying post-processing methods seems to be essential to modulate the issues relevant to these anomalies [6,7].

The surface defects are characterized by irregular surface features mainly caused by partially melted/unmelted powders, spatters, balling defects, melt-pool instability, stair-case effects, and support removal (SR) [8,9]. Moreover, design-related features such as geometrical complexity and the presence of overhanging surfaces with different orientations with respect to the build direction can significantly

influence the surface texture of L-PBF parts [10,11]. Based on the available data in the literature, most studies have considered un-notched standard specimens for characterizing the effect of surface texture on mechanical properties. On the other hand, notched AM parts exhibit more inhomogeneous surface texture because of the orientation of the downward and upward surfaces with respect to the build direction. While it has been reported that machining can be used to remove the surface defects from notched AM parts [12], machining of notched parts at the notch roots is quite challenging due to the geometrical constraints.

Other post-processing methods such as chemical surface treatments on the notched AM parts may be promising in addressing the issues related to surface anomalies. Generally, chemical treatments are highly efficient for the surface roughness reduction of AM materials [13,14]. In a previous study [15], the authors investigated the effects of different chemical treatments of chemical polishing (CP) and electro-chemical polishing (ECP) on the surface texture and fatigue behavior of V-notched L-PBF AlSi10Mg specimens with a notch root radius of 1 mm. The results revealed that the surface roughness of the notch root in the

* Corresponding author.

E-mail addresses: maleky.erfan@gamil.com, erfan.maleki@auburn.edu (E. Maleki).

<https://doi.org/10.1016/j.addlet.2023.100175>

Received 21 July 2023; Received in revised form 26 September 2023; Accepted 26 September 2023

Available online 27 September 2023

2772-3690/© 2023 The Authors. Published by Elsevier B.V. This is an open access article under the CC BY license (<http://creativecommons.org/licenses/by/4.0/>).

as-built state with $4.49 \mu\text{m}$ in terms of profile arithmetical roughness (R_a) was reduced to 3.19 and $2.96 \mu\text{m}$ after applying CP and ECP, respectively. Modifying the surface texture of the treated material resulted in fatigue life improvement at fixed stress amplitude of 110 MPa up to 11 and 17 times after CP and ECP, respectively, compared to the 1.26×10^4 cycles in the as-built surface condition. It should be noted that several studies have investigated the impact of severe plastic deformation methods on the surface texture of AM materials [16–18].

Herein, following our previous study, the effects of two different post-processing methods, T6 heat treatment (HT) and ECP, separate and combined, were studied on the porosity, microstructure, surface texture and mechanical properties, including fatigue, of U-notched L-PBF AlSi10Mg specimens with notch root radius of 0.25 mm . As the efficiency of post-processing methods is highly dependent on the geometry of the parts being processed, in this current study, we have focused on a different geometry, specifically U-notched specimens with a very narrow notch opening. This study introduces several pivotal novelties,

including the consideration of a new geometry, the examination of post-treatment effects on surface and fatigue behavior, and comprehensive microstructural characterization. Additionally, we conducted a pioneering numerical simulation on notched geometry exposed to various post-processing methods. The primary focus centered on evaluating the fatigue behavior of U-notched L-PBF AlSi10Mg parts. Subsequently, we embarked on assessing the efficacy of ECP in modifying the surface texture of this distinctive geometry.

2. Experimental procedure

For the fabrication of U-notched L-PBF AlSi10Mg specimens, argon gas atomized powder with a mean particle diameter of $44.5 \mu\text{m}$. Specimens were manufactured vertically via a SLM 500 HL system using the optimized process parameters of $78 \mu\text{m}$ spot diameter, 350 W laser power, 1150 mm/s scan speed, $50 \mu\text{m}$ layer thickness, $170 \mu\text{m}$ hatch distance, scanning strategy with 67° rotation between layers, and

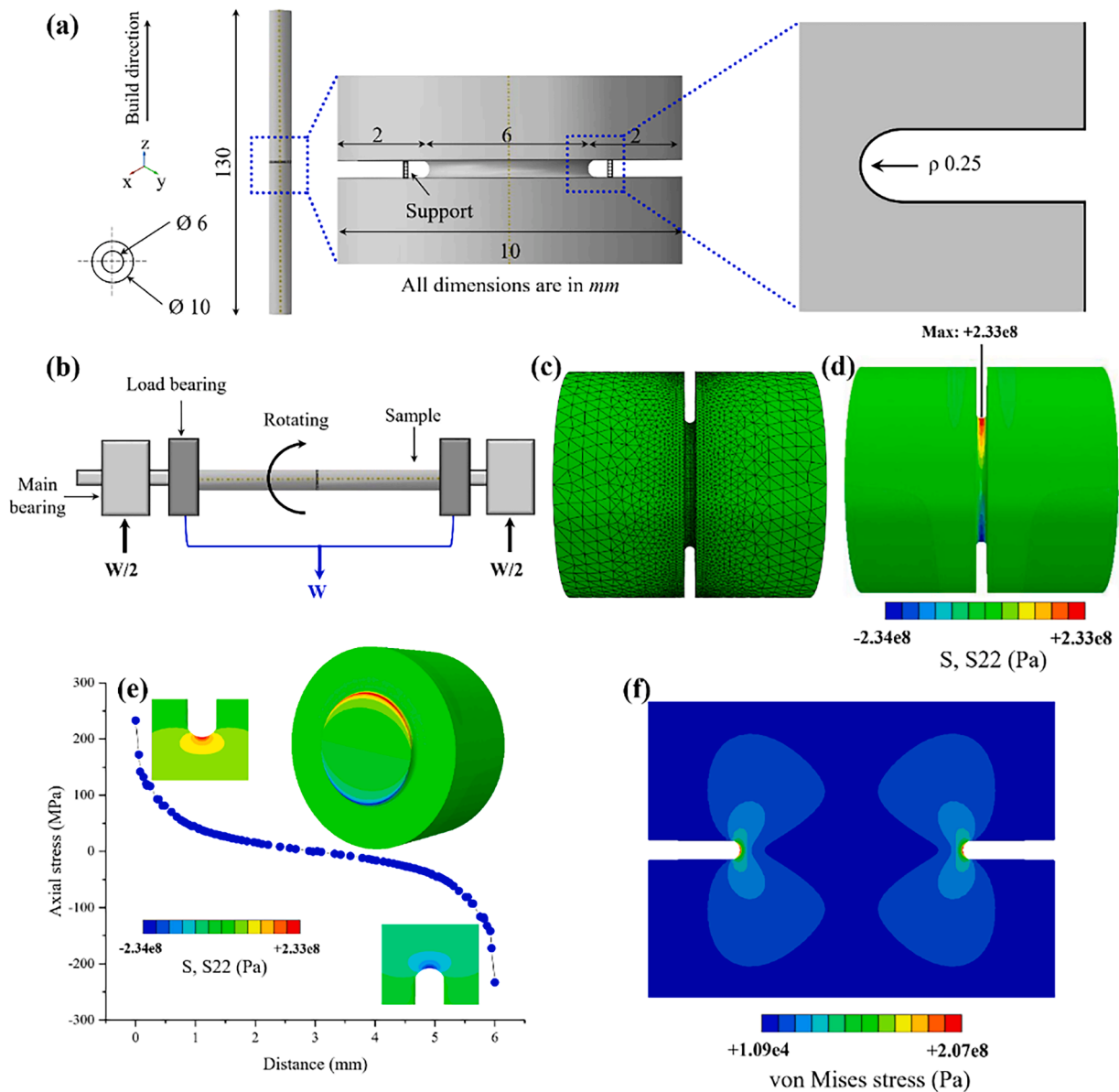


Fig. 1. (a) Shape and size of the U-notched L-PBF AlSi10Mg specimen with a narrow notch radius of 0.25 mm as well as the used supports for the fabrication process. (b) Schematic illustration of rotating bending fatigue setup. (c) Meshing of the notched area in the U-notched specimen. (d) Corresponding stress distribution in the minimum cross-section at notch root of the AD geometry considering 80 MPa bending load. (e) Values of axial stress distribution versus distance on notch root plane. (f) von-Mises stress distribution in the U-notched L-PBF AlSi10Mg part under 80 MPa bending load.

contour remelting. Fig. 1a depicts the shape and size of a cylindrical U-notched specimen with a narrow notch radius of 0.25 mm and notch width of 0.5 mm as well as the supports used for fabrication. It should be noted that SR was conducted manually using micro-cutters and tweezers.

Fatigue behavior assessment was carried out using Italsigma rotating bending fatigue test machine at three stress levels of 40, 60, and 80 MPa with a run-out limit of 5×10^6 cycles, stress ratio of $R = -1$, and rotational speed of about 2600 rpm with three specimens. Three specimens were tested at each stress level for each set. In addition, fractography was conducted on the failed specimens using a Zeiss EVO50 SEM. Fig. 1b presents a schematic illustration of the rotating bending fatigue test set-up. Linear elastic finite element analyses (FEA) were used to derive stress distributions within the notched plane, following the methodology reported by Maleki et al. [19]. FEA were performed using the commercial software Abaqus/Explicit 2019. The analysis utilized C3D10 quadratic tetrahedral elements, considering a cylindrical geometry with the diameter and notch design of the specimen as per the as-designed (AD) part. Fig. 1c and d reveal the considered meshing of the notched area and the corresponding stress distribution in the minimum cross-section at notch root with diameter of 6 mm of the AD geometry considering 80 MPa as one of the loads applied in the experiments, respectively. Following the results of the mesh convergence analysis, a total of 78,422 elements were employed. The values of axial stress distribution versus distance on notch root plane are illustrated in Fig. 1e. In addition, von-Mises stress distribution in the U-notched L-PBF part under 80 MPa bending load is depicted in Fig. 1f.

Addressing post-treatments, T6 thermal treatment, ECP, and a combination of these processes on the U-notched L-PBF AlSi10Mg specimens were conducted. Comprehensive information about the applied HT can be found in the work of Bagherifard et al. [20], while the optimized parameters for the ECP procedure were determined based on the findings from our prior researches [4,15]. While it is technically feasible to achieve precision machining of a 2-mm deep notch with a 0.25 mm radius, this task is undeniably challenging and demands specialized equipment and techniques, such as micro-machining. Nevertheless, due to the unavailability of such precise machining equipment and our specific objective to assess the effectiveness of ECP for geometries distinct from those examined in our prior research, we chose to employ ECP as the surface post-treatment method.

The microstructural characterizations were conducted following the steps presented by Maleki et al. [21] and AZtecHKL software was used to analyze the EBSD related data to generate microstructural maps.

Porosity measurements were performed using an image-based analysis approach. Firstly, several OM images were stitched to cover the specimens' whole cross-section in notched area and then ImageJ software [22] was used for analyzing the micrographs. In addition, non-local means and Gaussian noise filters were applied to obtain the Bernsen local thresholding in the binarized images to achieve a very high resolution [23–25]. Surface texture analyses were conducted using Zeiss EVO50 SEM to obtain the surface morphology and InfiniteFocus confocal microscope (with a lateral resolution of 0.10 μm and a vertical resolution of 10 nm) for roughness measurements. Rectangular areas of $0.7 \times 1 \text{ mm}^2$ below the notched area were scanned and nine acquisitions with 5 % overlap were collected for each specimen. Three different paths were considered for each roughness measurement and the average value was reported. The roughness parameters of R_a , root mean square (R_q), and maximum profile valley depth (R_v) were considered for surface roughness measurements following the ISO 25178-2 standard [26,27]. Additionally, in-depth microhardness tests and residual stress measurements were conducted in a manner consistent with the methods presented in our previous works [28].

3. Numerical simulation

2D finite FEA were performed on longitudinal cross-sections

obtained by EBSD scans to understand the effects of surface treatments on stress distribution considering the surface and near-surface defects. The scanned cross-sections, which had high resolutions to obtain all the surface and sub-surface features, were binarized using ImageJ software. Then, an in-house MATLAB code was utilized to create the part. The resulting part was imported into commercial FEA software, Abaqus/Explicit 2019, where the material was defined as linear elastic, isotropic and homogeneous. Monotonic stress-strain curve of L-PBF AlSi10Mg was used for the material model of as-built and heat treated states as suggested by Khajehmirza et al. [29]. During 2D meshing, an element type of CPS4R (linear quadrilateral) was employed, and the mesh was refined near the surfaces and defects. The procedure followed for FEA model setup for notch surfaces resulting from different post-processing conditions are shown in Fig. 2a–c. Boundary conditions at the bottom edge of the model were applied to constrain the vertical and horizontal displacement. A corresponding load to stress amplitude of 80 MPa (highest stress amplitude in the performed rotating bending fatigue tests) with linear distribution was applied to the notch cross-section to replicate the bending stress applied during rotating-bending fatigue tests along the y-axis. To ensure the accuracy of the results, mesh convergence analysis was conducted by using successively finer meshes and comparing the solution at each iteration. The process was continued until there were no significant changes in solution upon mesh refinement, as presented in Fig. 2d.

4. Results and discussions

4.1. Porosity analyses

In Fig. 3, the longitudinal cross-sections of all specimen sets are presented, with a specific focus on the notched regions. The obtained average porosity values for the different specimens were as follows: 0.61 % for AB, 0.59 % for AB+SR+ECP, 0.55 % for AB+HT, and 0.58 % for AB+HT+SR+ECP specimen. It's important to highlight that defects smaller than 10 μm were not detectable. These results provide clear insights, suggesting that neither the ECP nor the HT processes had a discernible effect on the porosity values within the specimens. The presence of sub-surface porosities around the notch root and near the notch's downward face could have implications for the mechanical properties and overall performance of the materials. Further investigations and analyses are warranted to explore the potential impact of these porosities on the structural integrity and durability of the specimens.

4.2. Surface texture analyses

In L-PBF parts, especially those with intricate geometries like notched components featuring both downward and upward surfaces, a higher prevalence of surface anomalies is typically observed. This is primarily attributed to the complex thermal history, reduced cooling rates, and the presence of overhangs, particularly on the downward-facing surfaces [30,31]. The qualitative comparison of these regions in U-notched L-PBF AlSi10Mg parts are presented in Fig. 4a using scanning electron microscopy (SEM). The results demonstrate the worst surface quality for the downward face with a high density of surface defects followed by the notch root and then the upward face. Surface roughness values of $R_a = 29.30, 9.40$, and $4.78 \mu\text{m}$ were obtained for downward face, notch root, and upward face, respectively. Our previous studies on V-notched L-PBF AlSi10Mg specimens [15,26,32] indicated that the surfaces of the notch roots exhibited the lowest content of surface anomalies. However, the results obtained in this study reveal that in the case of U-notched L-PBF AlSi10Mg parts, the upward-facing surfaces exhibited the least surface imperfections. This difference can be attributed to variations in geometry between U-notched and V-notched parts, resulting in different scanning strategies employed in the notched areas. Fig. 4b reveals the confocal observations of different surfaces in the

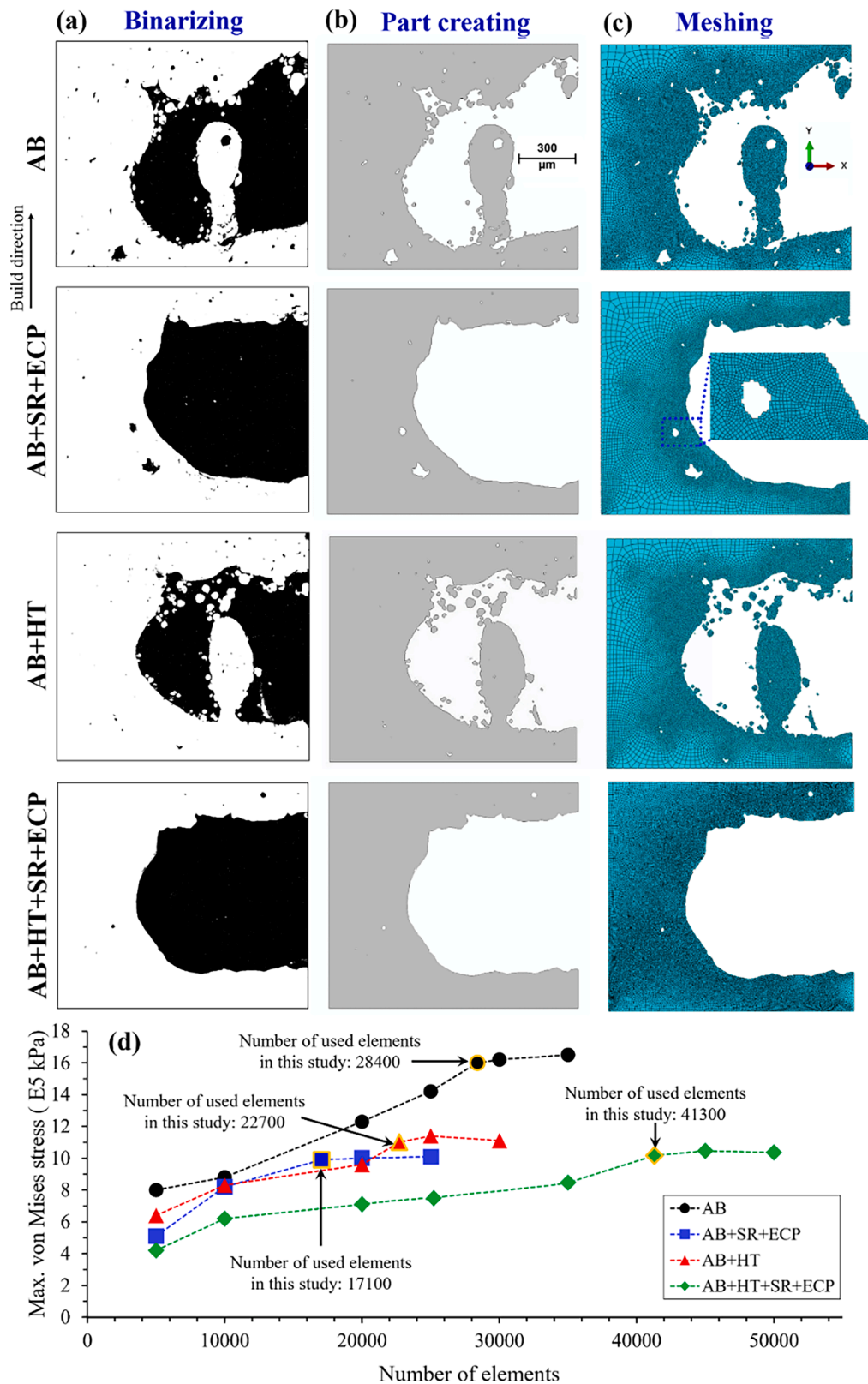


Fig. 2. Illustration of the steps followed to create the part for FEA under different post-processing conditions by (a) binarizing, (b) part creating and (c) meshing. (d) Results of mesh convergence analyses considering the effects of the number of elements on maximum von Mises stress.

U-notched region. Surface irregularities with a size of about 350 μm can be seen on the downward face. However, surface anomalies with maximum height of 250 and 150 μm were observed on the notch root and upward faces, respectively.

Surface morphologies of all sets of specimens including as-built and post-treated conditions were analyzed by SEM in notched area as presented in Fig. 4c–f. It can be observed that AB and AB+HT specimens have inferior surface quality due to the presence of irregular surface

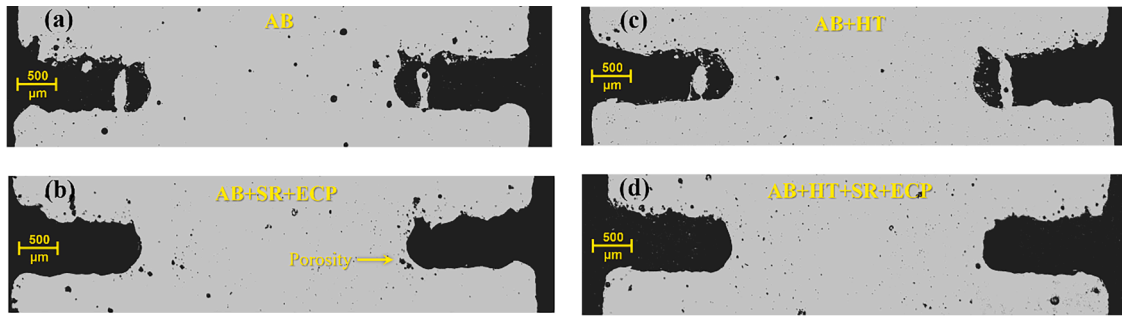


Fig. 3. Longitudinal cross-sections of the (a) AB, (b) AB + SR + ECP, (c) AB+HT, (d) AB+HT+SR+ECP specimens demonstrating sub-surface porosities around the notch regions.

anomalies, i.e., spatters, unmelted, and partially melted powders. Furthermore, it is evident that HT did not influence surface texture variations. The only discernible effect occurred in the AB+HT specimen, where localized surface irregularities led to a slight increase in the R_v value, which nonetheless remained comparable to the corresponding value in the AB specimen. After the application of ECP, nearly all of the surface irregularities present in the initial as-built and heat-treated states were successfully rectified. In the case of the AB+HT+SR+ECP specimen, the lower hardness/strength resulting from the heat treatment led to a heightened susceptibility to corrosion, resulting in the observation of relatively deep pits [33]. However, in the AB+SR+ECP specimen, a significant reduction in surface imperfections was achieved, with hardly any corrosion pits detected. Fig. 4e–j exhibit the surface texture of all sets of specimens obtained by confocal observations on the smooth area (cylindrical part below the notched area). It can be observed that more leveled surfaces without randomly positioned irregularities were obtained after applying ECP on both as-built and heat treated specimens. Surface roughness values of $R_a = 8.37, 3.31, 8.46$ and $3.21 \mu\text{m}$ were measured for AB, AB+SR+ECP, AB+HT and AB+HT+SR+ECP specimens, respectively, demonstrating considerable roughness reduction after applying ECP as illustrated in Fig. 4k. It should be mentioned that similar trends were also obtained for R_q and R_v surface roughness parameters. It should be noted that notch root diameter and the corresponding mass loss after ECP were measured for all sets as depicted in Fig. 4l demonstrating that the deviation from designed geometry was removed after ECP and notch root diameter of 6.04 and 6.01 were determined for AB+SR+ECP and AB+HT+SR+ECP respectively. Furthermore, it was observed that a higher mass loss of approximately 2.13 % was obtained following ECP treatment of the heat-treated state.

4.3. Microstructural characterization

Fig. 5 presents the OM observations exhibiting the typical microstructure of the AB and AB+HT specimens in transversal (xy -plane) and longitudinal (yz -plane) cross sections. In yz -plane of AB specimen, the melt pool morphologies and hatching lines, which elongated along the build direction can be seen. In the xy -plane of AB specimen the molten tracks and the inhomogeneous microstructure and melt pools with 67° rotation between the subsequent layers during fabrication can be observed. In contrast, in both the yz and xy -planes of the AB+HT specimen, all melt pool morphologies and hatching traces disappear indicating HT being effective in homogenizing the microstructure.

To further study the microstructure of the U-notched L-PBF AlSi10Mg specimens, the notch region was assessed by EBSD analysis on the transversal (xy -plane) cross-section as shown in Fig. 6. Crystallographic orientation in terms of inverse pole figure (IPF), grains size, Kernel average misorientation (KAM) and strain contouring (SC) maps were analyzed using EBSD data. Fig. 6a presents the IPF-Z maps in all sets demonstrating the domination of (001) orientation of the grains because of epitaxial growth of the grains along the build direction (Z)

[34–36]. The obtained results agree with the available data in the literature about the formation of columnar grains along the build direction in FCC metals [37], which leads to the formation of (001) fiber texture in AM state [38].

The formation of surface anomalies, including partially and unmelted powders as well as spatters on the downward face, notch root, and upward face of notches as well as sub-surface porosities in AB and AB+HT specimens, can be seen clearly in Fig. 6a. Dealing with specimens treated with ECP, it can be seen that the surface imperfections associated with the notch region were almost completely removed, resulting in highly modified surfaces. Fig. 6b shows the grain size distribution maps in the notch root of all sets of specimens. The results reveal that because of the manufacturing strategy with contouring, relatively larger grains were elongated in the notch root along the build direction. Within the imaged areas shown in Fig. 6b, the mean grain areas of 33.2, 28.3, 44.5 and $41.2 \mu\text{m}^2$ were measured for the AB, AB+SR+ECP, AB+HT, and AB+HT+SR+ECP specimens, respectively. Overall, the grains size became larger after applying HT, while a thin layer of notch root that had bigger elongated grains was removed by applying the ECP, leading to a slight reduction in average grain size.

Further microstructural analysis of the notched regions was conducted through KAM and SC maps, which can be used as indexes of stress concentration and strains, respectively [39–41], as shown in Fig. 7. Fig. 7a presents the KAM maps primarily considering the notch root in all sets exhibiting higher values in intersections of notch root and downward surfaces specified by yellow dashed shapes in the AB, AB+SR+ECP, and AB+HT specimens. The lowest mean KAM value was obtained for AB+HT+SR+ECP specimen with 0.50° followed by AB+HT, AB+SR+ECP, and AB specimens with $0.56, 0.61$ and 0.69° , respectively. Moreover, as shown in Fig. 7b, SC maps indicate higher maximum values of strains in the intersections of notch root and downward surfaces. Maximum values of localized plastic strains of 3.7, 3.4, 3.2 and 2.9 were measured for AB, AB+SR+ECP, AB+HT and AB+HT+SR+ECP specimens, respectively. Overall, KAM and SC maps analyses reveal that rather than the presence of residual stresses due to the rapid melting and cooling cycles during manufacturing by L-PBF [42], local stress concentration zones can be generated due to the complexity of fabricated part's geometry (such as U-notched specimens) that may affect the stress state in microstructural scale as well.

The FEA results are shown in Fig. 7c, exhibiting the stress distribution in the AD, AB and different post-processed conditions. As expected, in the case of AD specimen, stress is mainly distributed in the notch root region. While in the U-notched L-PBF AlSi10Mg specimens, stress distribution was more severe in the micro-notches at intersections of notch root and downward surfaces, especially for AB, AB+SR+ECP, and AB+HT specimens. Meanwhile, it was less pronounced for the AB+SR+HT+ECP specimen due to the reduced presence of the irregular features and micro-notches. Interestingly, stress distribution obtained from the FEA visually matched very well with the KAM and SC maps (dashed areas in Fig. 7a and b), highlighting that high misorientations and strains in microstructure are generated due to the complexity of the

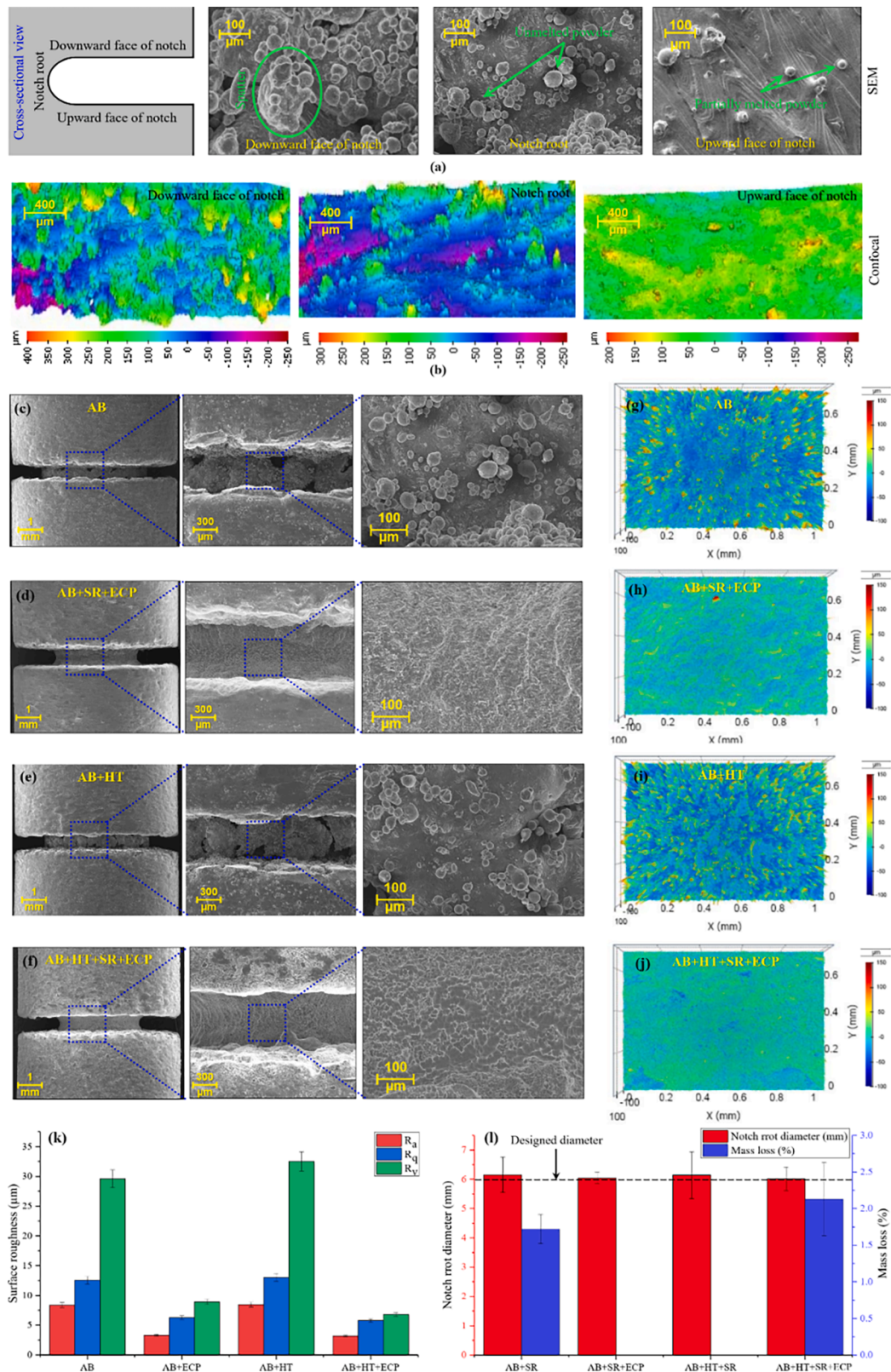


Fig. 4. (a) Schematic illustration of the locations of interest in the notch region, i.e., upward face, notch root, and downward face and the surface texture of different locations of a notch region obtained by SEM and (b) confocal observations. Surface morphologies of (c) AB, (d) AB+SR+ECP, (e) AB+HT, and (f) AB+HT+SR+ECP specimens taken from the notched area through SEM. The surface texture of (g) AB, (h) AB+SR+ECP, (i) AB+HT, and (j) AB+HT+SR+ECP obtained by confocal observations. (k) The measured surface roughness values in terms of R_a , R_q , and R_v for all sets. (l) The determined values of notch root diameter and the related mass loss after ECP in all sets.

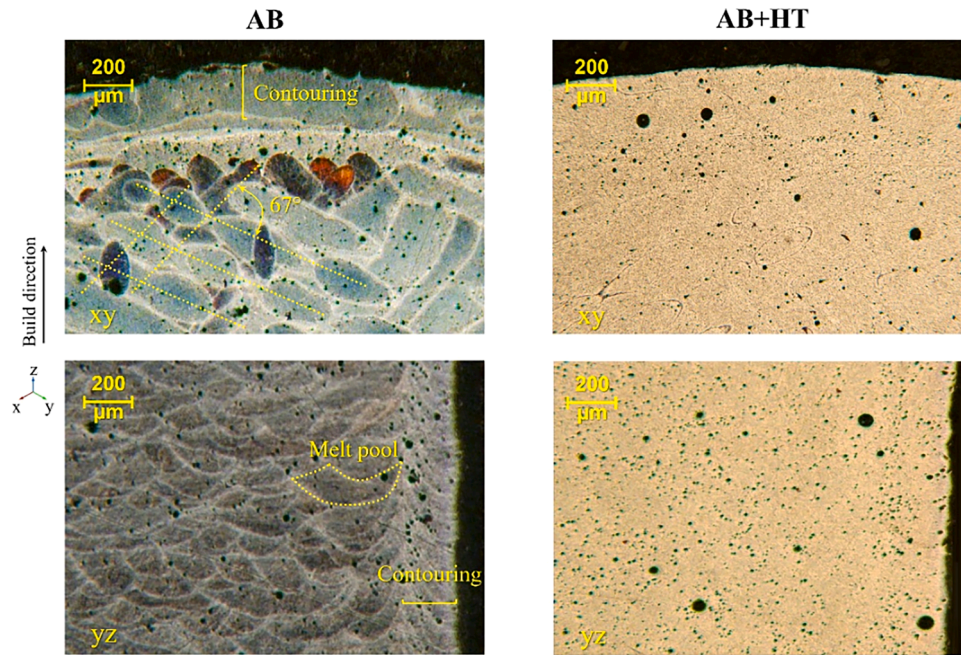


Fig. 5. Microstructure of AB (left) and AB+HT (right) specimens in transversal (xy-plane) and longitudinal (yz-plane) cross sections obtained by OM.

part' geometry fabricated by L-PBF. These areas were identified also by KAM and SC analyses as the high stress concentration zones, confirming that these zones are critical both regarding microstructure features and geometrical features. The observations derived from microstructural characterization and FEA analyses may not exhibit direct correlations, yet they are inherently linked to geometric factors that directly influence stress concentrations, cooling rates, and stress distribution. Notably, while FEA results were acquired post-loading, the SC and KAM results, obtained pre-loading, offer valuable insights into predicting stress concentration locations within the U-notched specimens. As SC and KAM do not require computational resources, they offer a rapid means of obtaining information about the critical locations of manufactured notched specimens. It can be also inferred from Fig. 7c that the response of U-notched L-PBF AlSi10Mg specimens to the fatigue loading is mainly sensitive to the surface of the notched area rather than internal defects and sub-surface porosities as relatively low stresses were observed near the pores. The results obtained from numerical simulations align with prior studies, which have consistently shown elevated stress concentrations in the micro-notches of AM materials when compared to smoother surfaces [43–46].

4.4. Mechanical properties

Regarding the effects of ECP on the mechanical properties of L-PBF materials, it was reported that this chemical process does not affect the hardness and residual stress distribution nor the tensile behavior [4,15]. Therefore, this study's microhardness and residual stresses measurements were only conducted on AB and AB+HT specimens. Some of the authors' recent study [28] revealed that after applying HT, the elongation of L-PBF AlSi10Mg increased compared to that of the as-built state. However, the yield and ultimate tensile strengths of the as-built state reduced down to 201 and 264 MPa, respectively, in the heat treated condition (see Fig. 8a). The microhardness profile obtained for the AB and AB+HT specimens is shown in Fig. 8b. It reveals that the heat-treated state resulted in a lower microhardness in the AB+HT condition due to microstructural changes.

The in-depth residual stresses distributions extracted from XRD analysis for AB and AB+HT specimens are shown in Fig. 8c. It can be observed that tensile residual stresses of as-built state with an average

value of 40 MPa were released and transformed to compressive residual stresses with a mean value of -31 MPa, which can highly affect the fatigue behavior. The results revealed a higher tensile residual values of about 60–70 MPa at a depth of 50–150 μm in the AB specimen, which is likely due to the application of contouring during fabrication and in agreement with another study [28].

The results of rotating bending fatigue tests at three different stress levels of 40, 60, and 80 MPa for all conditions are shown in Fig. 8d. It should be noted that SR was also conducted for AB and AB+HT specimens before fatigue tests. Compared to the AB set, it can be seen that AB+HT set, due to microstructural homogenization and improved ductility as well as residual stress relaxation, the specimens exhibited better fatigue performance. However, the AB+SR+ECP set, benefiting from chemical treatment, exhibited enhanced fatigue performance compared to the AB+HT set. This improvement can be attributed to reduced surface roughness, despite the presence of lower ductility and tensile residual stresses. These results reveal that the fatigue behavior of U-notched L-PBF AlSi10Mg specimens is more sensitive to the surface texture than microstructure and ductility. Additionally, it can be observed that AB+HT+SR+ECP set has the best fatigue performance compared to the other sets due to the beneficial outcomes of both thermal and chemical post-processing methods, such as homogenized microstructure, improved ductility, induced compressive residual stresses, and reduced surface roughness. Considering the treated sets with ECP in both the initial as-built and heat-treated states, at a higher stress amplitude of 80 MPa, the effects of surface modification fairly overshadowed the influence of improved ductility. The fatigue behavior was respectively enhanced up to 4.3 and 5.3 times compared to the AB set, which does not represent a significant difference. However, at a lower stress amplitude of 40 MPa, the effects of improved ductility became more pronounced. The fatigue life was notably improved by applying HT+ECP, increasing it by 255 times compared to the as-built condition. This represents a considerable difference, especially when compared to the 119-fold improvement achieved by ECP alone.

Fig. 8e–h illustrate the fracture surfaces of the specimens after the fatigue tests observed by SEM. Similar patterns of fatigue failure with multiple crack initiation sites can be seen for all sets, which is typical for notched geometry. Failure started from all around the section representing uniform circumferential cracks similar to the results presented in

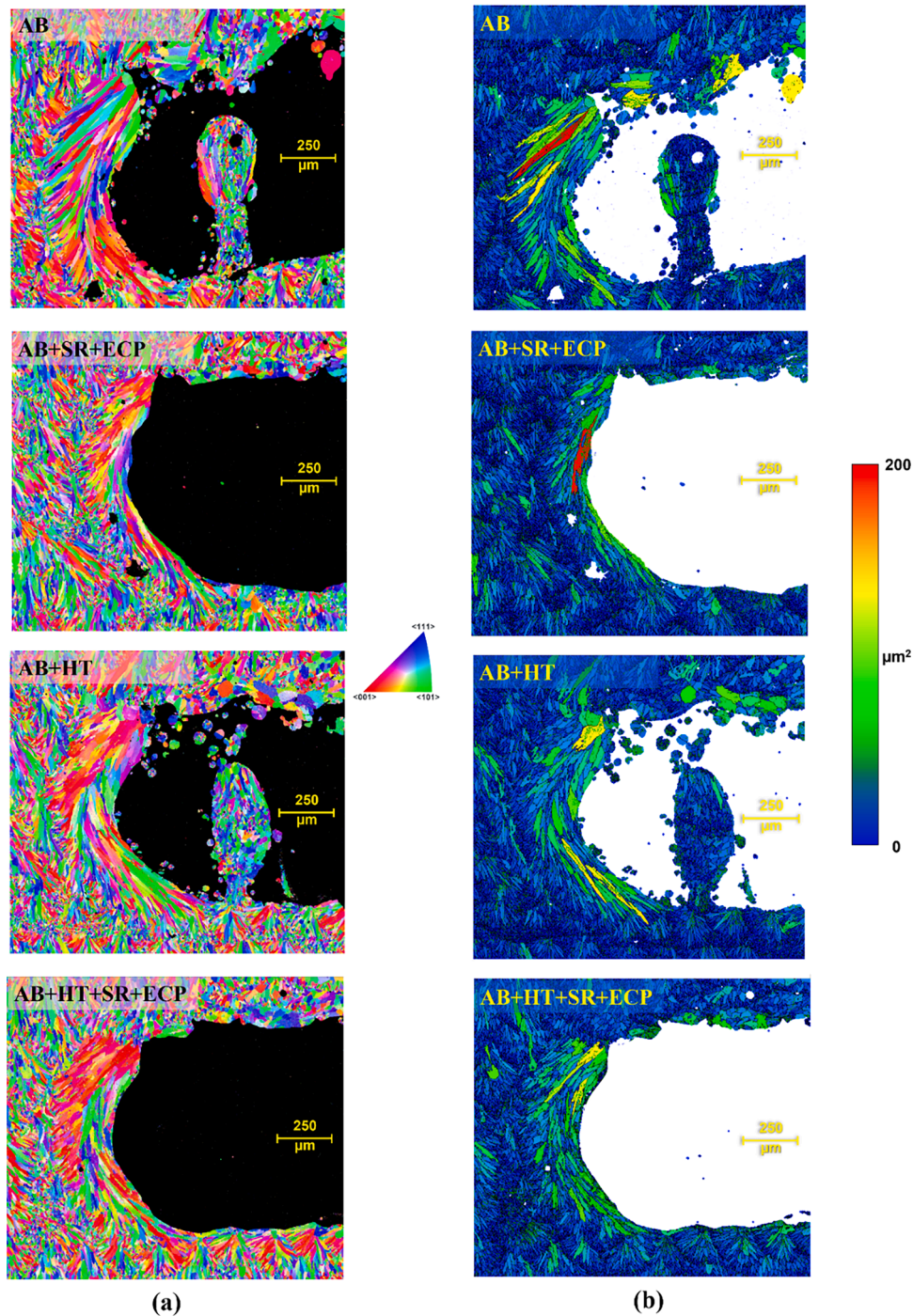


Fig. 6. EBSD results in terms of (a) IPF-Z and (b) grain size distribution maps in all sets focusing on the notch areas.

previous studies [20,47]. In all sets, an asymmetric fracture surface feature was noted where a dominating surface crack nucleated and propagated through the majority of the fracture plane. In addition, in a few cases, the crack initiations were affected by the presence of near-surface pores. Overall, it can be observed that the cracks nucleated from the surface anomalies, especially the valleys. Even in the heat treated sets, the contribution of the surface defects around the notch region to the final failure seems higher than the improved ductility. These results confirm that the fatigue behavior of U-notched L-PBF AlSi10Mg specimens under rotating bending fatigue loading is very sensitive to the surface morphology. The depth of these valleys, known to have negative effects on fatigue behavior, underwent significant

reduction and, in certain instances, were fully eliminated because of the application of chemical post-processing. The reduction or elimination of these detrimental valleys played a crucial role in enhancing fatigue performance beyond what could be solely attributed to improved ductility. It should be noted that in metals AM, the coexistence of defects, notches, and rough surfaces can lead to a hardening effect, potentially diminishing ductility in the vicinity of the notch and negatively impacting overall mechanical performance compared to wrought metals, even though the metal is generally expected to exhibit ductile behavior [48].

Recent studies on notched AM parts have highlighted that while theoretically, the notch root is expected to have the highest stress

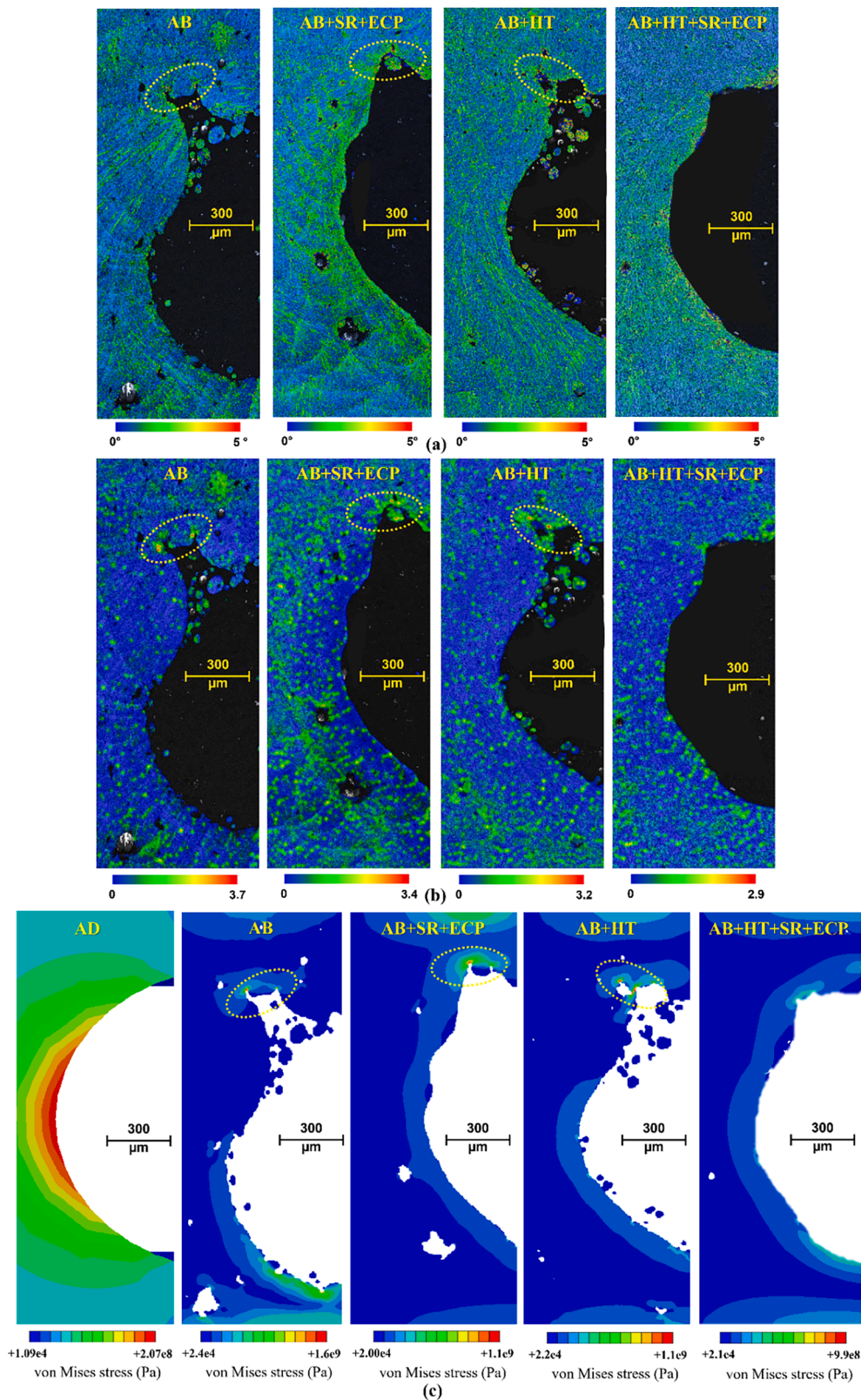


Fig. 7. EBSD analyses results for all sets of specimens in terms of (a) KAM and (b) SC maps. (c) FEA results in terms of distribution of von Mises stress after loading at fixed applied stress of 80 MPa for all sets.

concentration in the component, it doesn't always serve as the site of fatigue failure. Instead, fatigue fractures have been observed to predominantly initiate close to downward face of the notch. This phenomenon can be attributed to factors such as elevated surface roughness

and the presence of potential crack nucleation sites in that area. The parameter of relative height (h/h_0) is used to determine the locations of fracture sites, and it can be calculated as the ratio of the distance from the failure initiation site to the notch root (h) divided by the total notch

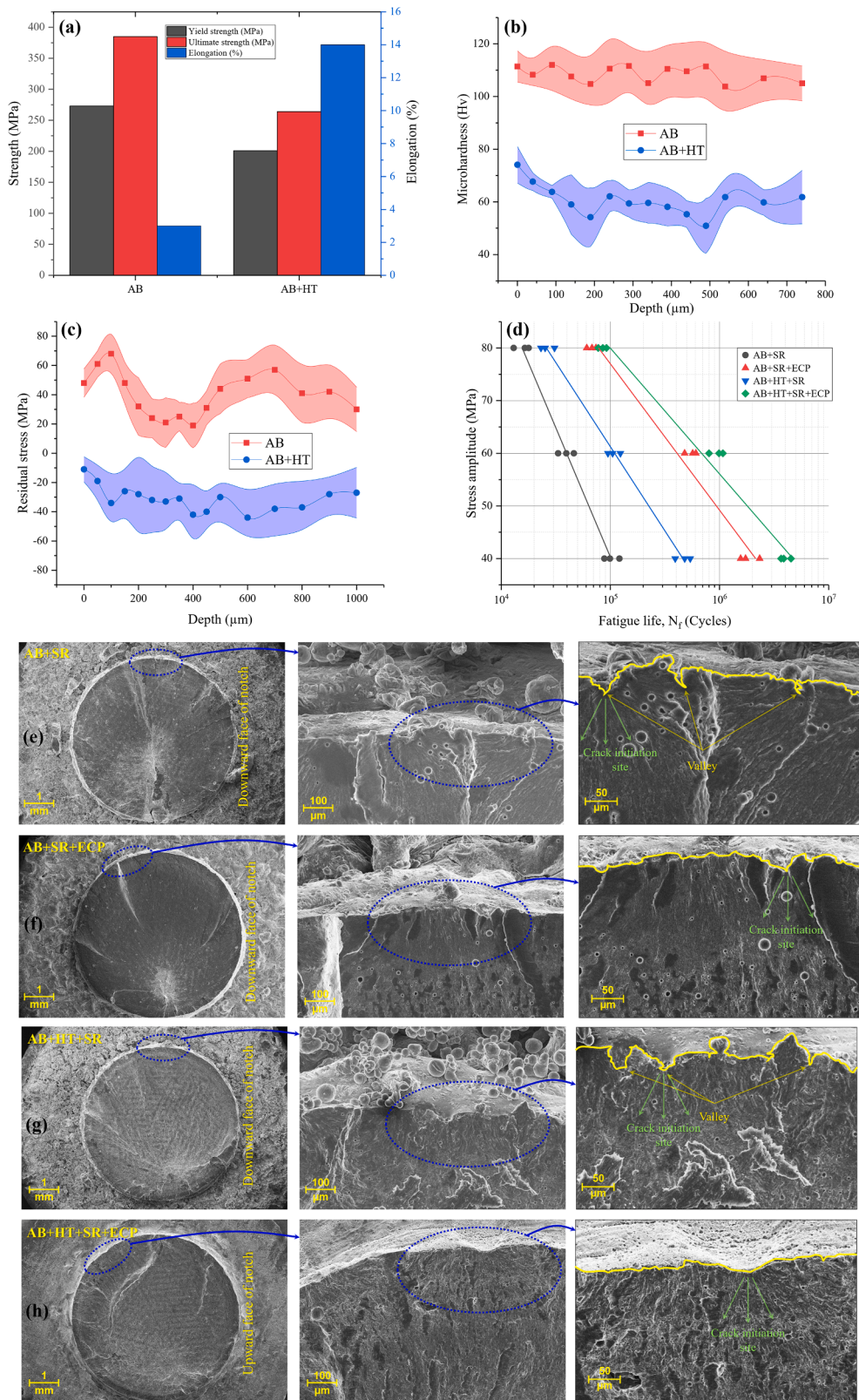


Fig. 8. Mechanical properties of as-built and heat treated states in terms of (a) tensile behavior, which adopted from [28], (b) microhardness, and (c) residual stresses distribution. (d) Fatigue test results of U-notched L-PBF AlSi10Mg specimens at three different stress levels of 40, 60, and 80 MPa. Fracture surfaces of (e) AB+SR, (f) AB+SR+ECP, (g) AB+HT+SR and (h) AB+HT+SR+ECP specimens after fatigue tests at 60 MPa stress amplitude observed by SEM.

opening (h_0). Fig. 9a reveals the schematic illustration of relative height of fracture site in U-notched and V-notched geometries. To investigate the impact of applied post-processing methods on the variation of fracture sites and to validate our findings concerning the correlation between severe stress concentration zones in the micro-notches at the intersections of the notch root and downward surfaces (as depicted in Fig. 7) with fracture locations, relative height of fracture sites for all broken specimens across all sets were determined as shown in Fig. 9b. The results indicate that post-treatments have a considerable impact on the fracture site's location, causing it to shift towards the direction of the notch root. When evaluating the individual effects of the applied post-treatments, it is evident that ECP demonstrates higher efficiency than HT in moving the fracture site closer to the notch root. Furthermore, it is noteworthy that all fracture sites across all specimens are positioned higher than the notch root direction and in closer proximity to the downward surface. Additionally, a clear trend emerges as the stress amplitude increases, the relative height values also enhance which has high agreement with presented data in the literature [49]. The results highlight a particularly interesting observation, specifically for the AB+SR and AB+HT+SR specimens, where the fracture sites align closely with the intersections of the notch root and downward surfaces. While in the treated specimens with ECP, where the severity of stress concentrations on surface micro-notches is lower, the fracture site exhibited a slight downward shift from the intersections of the notch

root and downward surfaces. This aligns well with our findings that indicated the highest stress concentration in that region.

In addition, to enhance our comprehension of the effects of geometry and post-treatments, the results obtained from our previous study on V-notched L-PBF AlSi10Mg [15], regarding fracture site characteristics were presented. It is apparent that the relative height of fracture sites in the fabricated U-notched specimens remains higher than those in V-notched specimens, even after the application of post-treatments. This discrepancy can be attributed to the challenging surface quality inherent to the considered U-notch geometry. Notably, only in the case of the AB+HT+SR+ECP specimen under a 40 MPa loading condition, the relative heights approximately align within the same range as the ones in V-notched geometry.

Moreover, as depicted in Fig. 9c, the pattern of relocating the relative height of the fracture site after ECP is also observable in SEM fractographies. For example, in the highlighted region of the fracture surface for the AB+SR specimen, the fracture plane is very proximate to the interface of the notch root and downward surface. However, in the AB+SR+ECP specimen, this distance is greater, indicating that the relative height of the fracture site has shifted downward. This observation aligns with the findings presented in Figs. 7 and 9b.

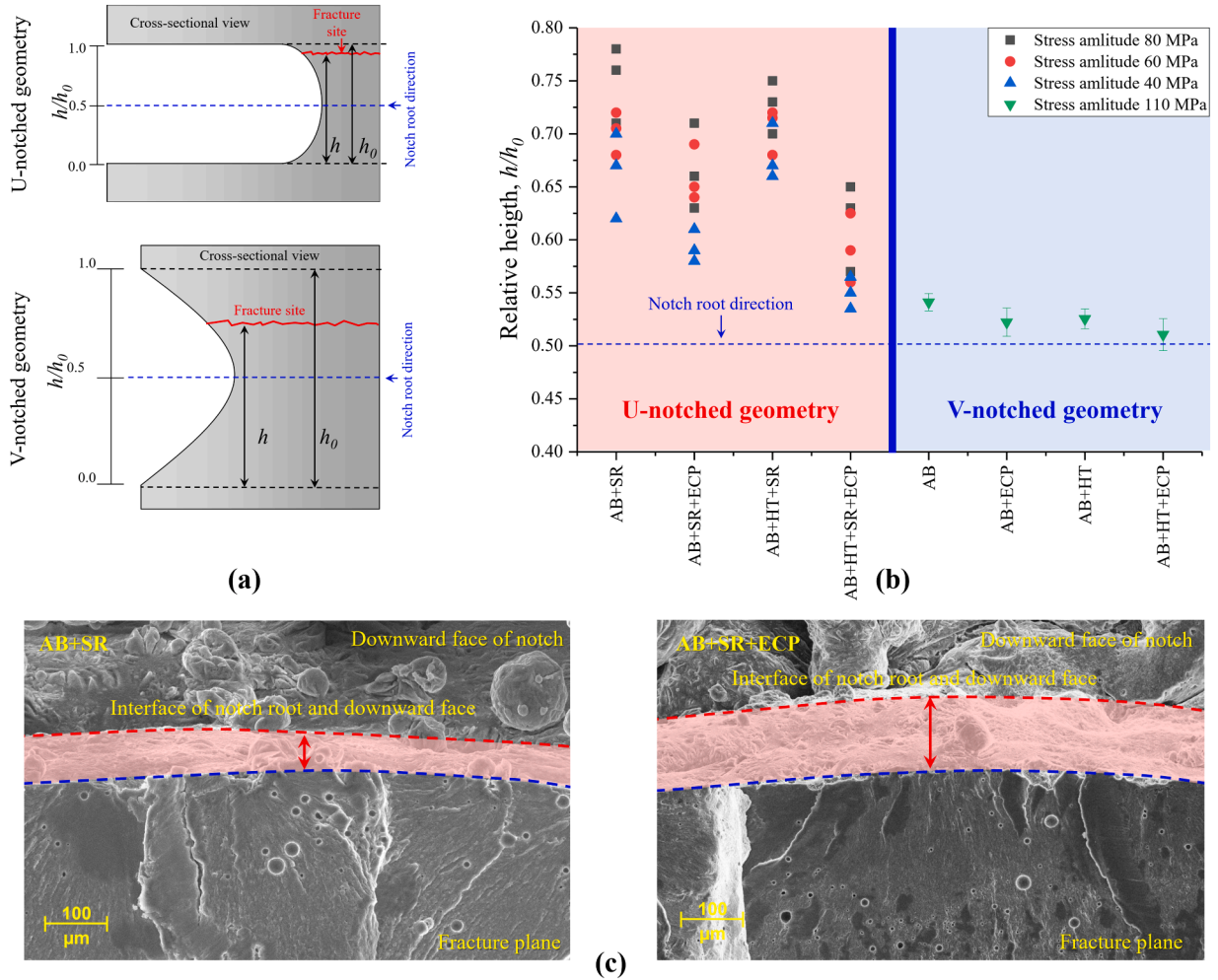


Fig. 9. (a) Schematic illustrations of relative height of fracture sites in U-notched and V-notched geometries. (b) The obtained relative heights of all U-notched specimens under different loadings of 40, 60 and 80 MPa. Also, relative heights of V-notched specimens adopted from our previous study [15] were illustrated for comparison. (c) Comparison of the distance of fracture plane and downward face of notch for AB+SR and AB+SR+ECP specimens demonstrating the relocating the relative height of the fracture site after ECP.

5. Conclusions

In this study the effects of separate ECP and HT treatments, as well as their combination on the surface morphology, porosity, microstructure, mechanical properties, and fatigue behavior of U-notched L-PBF AlSi10Mg specimens were experimentally investigated. In addition, FEA were conducted to better understand the effects of applied post-processing methods on stress distribution considering the surface and near-surface defects in the notch area. Based on the obtained results, the following conclusions can be drawn:

- ECP was found to be an effective post-treatment for surface texture modification and roughness reduction for narrow notched geometries for which applying other surface post-treatments is challenging or impossible. Surface roughness was reduced to about 60 % after applying ECP.
- HT, rather than increasing the ductility, homogenized the microstructure, released the tensile residual stresses with a mean value of 40 MPa in as-built specimens to compressive residual stresses with an average value of −31 MPa.
- The stress concentration was more severe in the micro-notches at notch root and downward surfaces intersections based on the microstructural characterizations before any loading. Interestingly, the obtained stress concentration zones from the FEA after loading matched microstructural maps very well. The identified areas as the high stress concentration zones, confirming that these zones are critical both regarding microstructure features and geometrical features.
- Based on the results of numerical simulation, it was also found that the response of U-notched L-PBF AlSi10Mg specimens to the fatigue loading was sensitive primarily to the surface quality of the notched area rather than the sub-surface porosities.
- Both HT and ECP positively affected the specimen's fatigue behavior; the hybrid treatment of HT+ECP had the highest influence on fatigue behavior improvement, followed by sole treatments of ECP and HT, respectively. It was also found that the fatigue behavior of the U-notched L-PBF AlSi10Mg specimens was more sensitive to the surface morphology rather than microstructure and ductility. In the ECP treated sets with both initial as-built and heat treated states, the effects of surface modification relatively masked the influence of improved ductility at higher stress amplitudes. While at lower stress amplitudes, the effect of enhanced ductility was more evident.
- The results regarding the relative heights of fracture sites indicate that, across all specimens, these sites are situated higher than the notch root direction and in closer proximity to the downward surface. Notably, in the case of the AB+SR and AB+HT+SR specimens, the fracture sites closely align with the intersections of the notch root and downward surfaces, consistent with our earlier findings that identified the highest stress concentration in this region.

CRedit authorship contribution statement

Erfan Maleki: Conceptualization, Investigation, Formal analysis, Visualization, Writing – original draft, Supervision, Project administration. **Sara Bagherifard:** Conceptualization, Methodology, Data curation, Validation, Writing – review & editing, Supervision. **Nabeel Ahmad:** Investigation, Formal analysis, Software, Writing – original draft. **Shuai Shao:** Formal analysis, Writing – review & editing. **Okan Unal:** Methodology, Investigation, Formal analysis, Data curation. **Mario Guagliano:** Resources, Writing – review & editing, Supervision, Project administration. **Nima Shamsaei:** Funding acquisition, Resources, Writing – review & editing.

Declaration of Competing Interest

The authors declare that they have no known competing financial

interests or personal relationships that could have appeared to influence the work reported in this paper.

Data availability

Data will be made available on request.

Acknowledgment

This material is based upon work partially supported by the National Institute of Standards and Technology (NIST) under Award No. 70NANB19H170.

References

- [1] D. Herzog, V. Seyda, E. Wycisk, C. Emmelmann, Additive manufacturing of metals, *Acta Mater.* 117 (2016) 371–392, <https://doi.org/10.1016/j.actamat.2016.07.019>.
- [2] I. Yadroitsev, I. Smurov, Surface morphology in selective laser melting of metal powders, in: *Phys. Procedia*, 2011, pp. 264–270, <https://doi.org/10.1016/j.phpro.2011.03.034>.
- [3] Z. Xu, A. Liu, X. Wang, Fatigue performance and crack propagation behavior of selective laser melted AlSi10Mg in 0°, 15°, 45° and 90° building directions, *Mater. Sci. Eng. A* 812 (2021), <https://doi.org/10.1016/j.msea.2021.141141>.
- [4] E. Maleki, S. Bagherifard, O. Unal, F. Sabouri, M. Bandini, M. Guagliano, Effects of different mechanical and chemical surface post-treatments on mechanical and surface properties of as-built laser powder bed fusion AlSi10Mg, *Surf. Coatings Technol.* 439 (2022), 128391, <https://doi.org/10.1016/j.surfcoat.2022.128391>.
- [5] J. Pegues, M. Roach, R. Scott Williamson, N. Shamsaei, Surface roughness effects on the fatigue strength of additively manufactured Ti-6Al-4V, *Int. J. Fatigue* 116 (2018) 543–552, <https://doi.org/10.1016/j.ijfatigue.2018.07.013>.
- [6] E. Maleki, S. Bagherifard, M. Bandini, M. Guagliano, Surface post-treatments for metal additive manufacturing: progress, challenges, and opportunities, *Addit. Manuf.* 37 (2021), 101619, <https://doi.org/10.1016/j.addma.2020.101619>.
- [7] S. Lee, S. Shao, D.N. Wells, M. Zetek, M. Kepka, N. Shamsaei, Fatigue behavior and modeling of additively manufactured IN718: the effect of surface treatments and surface measurement techniques, *J. Mater. Process. Technol.* 302 (2022), 117475, <https://doi.org/10.1016/j.jmatprotec.2021.117475>.
- [8] M.H. Nasab, D. Gastaldi, N.F. Lecis, M. Vedani, On morphological surface features of the parts printed by selective laser melting (SLM), *Addit. Manuf.* 24 (2018) 373–377, <https://doi.org/10.1016/j.addma.2018.10.011>.
- [9] Z. Zhang, C. Sun, X. Xu, L. Liu, Surface quality and forming characteristics of thin-wall aluminum alloy parts manufactured by laser assisted MIG arc additive manufacturing, *Int. J. Light. Mater. Manuf.* 1 (2018) 89–95, <https://doi.org/10.1016/j.ijlmm.2018.03.005>.
- [10] N.E. Uzan, S. Ramati, R. Shneck, N. Frage, O. Yeheskel, On the effect of shot-peening on fatigue resistance of AlSi10Mg specimens fabricated by additive manufacturing using selective laser melting (AM-SLM), *Addit. Manuf.* 21 (2018) 458–464, <https://doi.org/10.1016/j.addma.2018.03.030>.
- [11] A. Leon, E. Aghion, Effect of surface roughness on corrosion fatigue performance of AlSi10Mg alloy produced by Selective Laser Melting (SLM), *Mater. Charact.* 131 (2017) 188–194, <https://doi.org/10.1016/j.matchar.2017.06.029>.
- [12] T.D. McLouth, D.B. Witkin, J.R. Lohser, G.E. Bean, S.D. Sitzman, P.M. Adams, J. M. Yang, R.J. Zaldivar, Elevated temperature notch sensitivity of Inconel 718 manufactured by selective laser melting, *J. Mater. Eng. Perform.* 30 (2021) 4882–4890, <https://doi.org/10.1007/s11665-021-05522-9>.
- [13] S.M. Ahmadi, R. Kumar, E.V. Borisov, R. Petrov, S. Leeftang, Y. Li, N. Tümer, R. Huizenga, C. Ayas, A.A. Zadpoor, V.A. Popovich, From microstructural design to surface engineering: a tailored approach for improving fatigue life of additively manufactured meta-biomaterials, *Acta Biomater.* 83 (2019) 153–166, <https://doi.org/10.1016/j.actbio.2018.10.043>.
- [14] B. Wysocki, J. Idaszek, J. Buhagiar, K. Szlázak, T. Brynk, K.J. Kurzydowski, W. Świążkowski, The influence of chemical polishing of titanium scaffolds on their mechanical strength and in-vitro cell response, *Mater. Sci. Eng. C* 95 (2019) 428–439, <https://doi.org/10.1016/j.msec.2018.04.019>.
- [15] E. Maleki, S. Bagherifard, F. Sabouri, M. Bandini, M. Guagliano, Hybrid thermal, mechanical and chemical surface post-treatments for improved fatigue behavior of laser powder bed fusion AlSi10Mg notched samples, *Surf. Coatings Technol.* 430 (2022), 127962, <https://doi.org/10.1016/j.surfcoat.2021.127962>.
- [16] D.A. Lesyk, S. Martinez, B.N. Mordyuk, V.V. Dzhemelinskiy, Lamikiz, G. I. Prokopenko, Post-processing of the Inconel 718 alloy parts fabricated by selective laser melting: effects of mechanical surface treatments on surface topography, porosity, hardness and residual stress, *Surf. Coatings Technol.* (2020), <https://doi.org/10.1016/j.surfcoat.2019.125136>.
- [17] E. Maleki, O. Unal, M. Bandini, M. Guagliano, S. Bagherifard, Individual and synergistic effects of thermal and mechanical surface post-treatments on wear and corrosion behavior of laser powder bed fusion AlSi10Mg, *J. Mater. Process. Technol.* 302 (2022), 117479, <https://doi.org/10.1016/j.jmatprotec.2021.117479>.
- [18] E. Maleki, S. Bagherifard, A. Heydari Astaraee, S. Sgarbazzini, M. Bandini, M. Guagliano, Application of gradient severe shot peening as a novel mechanical

- surface treatment on fatigue behavior of additively manufactured AlSi10Mg, *Mater. Sci. Eng. A* (2023), <https://doi.org/10.1016/j.msea.2023.145397>.
- [19] E. Maleki, S. Bagherifard, M. Guagliano, Correlation of residual stress, hardness and surface roughness with crack initiation and fatigue strength of surface treated additive manufactured AlSi10Mg: experimental and machine learning approaches, *J. Mater. Res. Technol.* 24 (2023) 3265–3283, <https://doi.org/10.1016/j.jmrt.2023.03.193>.
- [20] S. Bagherifard, N. Beretta, S. Monti, M. Riccio, M. Bandini, M. Guagliano, On the fatigue strength enhancement of additive manufactured AlSi10Mg parts by mechanical and thermal post-processing, *Mater. Des.* 145 (2018) 28–41, <https://doi.org/10.1016/j.matdes.2018.02.055>.
- [21] E. Maleki, S. Bagherifard, L. Rovatti, R. Michael, M. Revuru, M. Guagliano, Developing a best practice for sample preparation of additive manufactured AlSi10Mg for electron backscatter diffraction analysis, *Addit. Manuf. Lett.* 5 (2023), 100122, <https://doi.org/10.1016/j.addlet.2023.100122>.
- [22] C.A. Schneider, W.S. Rasband, K.W. Eliceiri, NIH Image to ImageJ: 25 years of image analysis, *Nat. Methods* 9 (2012) 671–675, <https://doi.org/10.1038/nmeth.2089>.
- [23] F.H. Kim, S.P. Moylan, E.J. Garboczi, J.A. Slotwinski, Investigation of pore structure in cobalt chrome additively manufactured parts using X-ray computed tomography and three-dimensional image analysis, *Addit. Manuf.* 17 (2017) 23–38, <https://doi.org/10.1016/j.addma.2017.06.011>.
- [24] J. Bernsen, Dynamic thresholding of grey-level images, in: *Proc. - Int. Conf. Pattern Recognit.*, 1986, pp. 1251–1255.
- [25] E. Maleki, S. Bagherifard, O. Unal, M. Bandini, M. Guagliano, The effects of microstructural and chemical surface gradients on fatigue performance of laser powder bed fusion AlSi10Mg, *Mater. Sci. Eng. A* 840 (2022), 142962, <https://doi.org/10.1016/j.msea.2022.142962>.
- [26] E. Maleki, S. Bagherifard, S.M.J. Razavi, M. Riccio, M. Bandini, A. du Plessis, F. Berto, M. Guagliano, Fatigue behaviour of notched laser powder bed fusion AlSi10Mg after thermal and mechanical surface post-processing, *Mater. Sci. Eng. A* 829 (2022), 142145, <https://doi.org/10.1016/j.msea.2021.142145>.
- [27] International Organization for Standardization, ISO 25178-2: geometrical product specifications (GPS) - Surface texture: areal Part - 2: terms, definitions and surface texture parameters, 2007.
- [28] E. Maleki, S. Bagherifard, O. Unal, S. Shao, N. Shamsaei, Assessing the efficacy of several impact-based mechanical techniques on fatigue behavior of additive manufactured AlSi10Mg, *Mater. Sci. Eng. A* 872 (2023), 144940, <https://doi.org/10.1016/j.msea.2023.144940>.
- [29] H. Khajehmirza, A.H. Astaraee, S. Monti, M. Guagliano, S. Bagherifard, A. Heydari Astaraee, S. Monti, M. Guagliano, S. Bagherifard, A hybrid framework to estimate the surface state and fatigue performance of laser powder bed fusion materials after shot peening, *Appl. Surf. Sci.* 567 (2021), 150758, <https://doi.org/10.1016/j.apsusc.2021.150758>.
- [30] S.M.J. Razavi, P. Ferro, F. Berto, J. Torgersen, Fatigue strength of blunt V-notched specimens produced by selective laser melting of Ti-6Al-4V, *Theor. Appl. Fract. Mech.* 97 (2018) 376–384, <https://doi.org/10.1016/j.tafmec.2017.06.021>.
- [31] A. Yadollahi, N. Shamsaei, Additive manufacturing of fatigue resistant materials: challenges and opportunities, *Int. J. Fatigue* 98 (2017) 14–31, <https://doi.org/10.1016/j.ijfatigue.2017.01.001>.
- [32] E. Maleki, S. Bagherifard, O. Unal, M. Bandini, M. Guagliano, On the effects of laser shock peening on fatigue behavior of V-notched AlSi10Mg manufactured by laser powder bed fusion, *Int. J. Fatigue* 163 (2022), 107035, <https://doi.org/10.1016/j.ijfatigue.2022.107035>.
- [33] E. Maleki, S. Bagherifard, O. Unal, M. Revuru, M. Bandini, M. Guagliano, The efficiency of tumble finishing as a final post-treatment for fatigue enhancement of notched laser powder bed fusion AlSi10Mg, *Sci. Rep.* 13 (2023) 4602, <https://doi.org/10.1038/s41598-023-30660-6>.
- [34] A. Hadadzadeh, B.S. Amirkhiz, J. Li, M. Mohammadi, Columnar to equiaxed transition during direct metal laser sintering of AlSi10Mg alloy: effect of building direction, *Addit. Manuf.* 23 (2018) 121–131, <https://doi.org/10.1016/j.addma.2018.08.001>.
- [35] A. Basak, S. Das, Epitaxy and microstructure evolution in metal additive manufacturing, *Annu. Rev. Mater. Res.* 46 (2016) 125–149, <https://doi.org/10.1146/annurev-matsci-070115-031728>.
- [36] L. Thijs, K. Kempen, J.P. Kruth, J. Van Humbeeck, Fine-structured aluminium products with controllable texture by selective laser melting of pre-alloyed AlSi10Mg powder, *Acta Mater.* 61 (2013) 1809–1819, <https://doi.org/10.1016/j.actamat.2012.11.052>.
- [37] Y.J. Liu, Z. Liu, Y. Jiang, G.W. Wang, Y. Yang, L.C. Zhang, Gradient in microstructure and mechanical property of selective laser melted AlSi10Mg, *J. Alloys Compd.* 735 (2018) 1414–1421, <https://doi.org/10.1016/j.jallcom.2017.11.020>.
- [38] N. Takata, H. Kodaira, A. Suzuki, M. Kobashi, Size dependence of microstructure of AlSi10Mg alloy fabricated by selective laser melting, *Mater. Charact.* 143 (2018) 18–26, <https://doi.org/10.1016/j.matchar.2017.11.052>.
- [39] A. Ramazani, K. Mukherjee, A. Schwedt, P. Goravanchi, U. Pahl, W. Bleck, Quantification of the effect of transformation-induced geometrically necessary dislocations on the flow-curve modelling of dual-phase steels, *Int. J. Plast.* 43 (2013) 128–152, <https://doi.org/10.1016/j.ijplas.2012.11.003>.
- [40] J. Kadkhodapour, S. Schmauder, D. Raabe, S. Ziaei-Rad, U. Weber, M. Calcagnotto, Experimental and numerical study on geometrically necessary dislocations and non-homogeneous mechanical properties of the ferrite phase in dual phase steels, *Acta Mater.* 59 (2011) 4387–4394, <https://doi.org/10.1016/j.actamat.2011.03.062>.
- [41] O. Unal, E. Maleki, I. Karademir, F. Husem, Y. Efe, T. Das, Effects of conventional shot peening, severe shot peening, re-shot peening and precision grinding operations on fatigue performance of AISI 1050 railway axle steel, *Int. J. Fatigue* 155 (2022), <https://doi.org/10.1016/j.ijfatigue.2021.106613>.
- [42] A. Tajyar, N. Brooks, N. Holtham, R. Rowe, D.J. Newell, A.N. Palazotto, K. Davami, Effects of a modified heat-treatment on microstructure and mechanical properties of additively manufactured Inconel 718, *Mater. Sci. Eng. A* (2022), <https://doi.org/10.1016/j.msea.2022.142770>.
- [43] T.D. Dinh, J. Vanwallegem, H. Xiang, H. Erdelyi, T. Craeghs, W. Van Paepegem, A unified approach to model the effect of porosity and high surface roughness on the fatigue properties of additively manufactured Ti6-Al4-V alloys, *Addit. Manuf.* (2020), <https://doi.org/10.1016/j.addma.2020.101139>.
- [44] A. Sombatmai, V. Uthaisangsuk, S. Wongwises, P. Promopattum, Multiscale investigation of the influence of geometrical imperfections, porosity, and size-dependent features on mechanical behavior of additively manufactured Ti-6Al-4V lattice struts, *Mater. Des.* (2021), <https://doi.org/10.1016/j.matdes.2021.109985>.
- [45] T.D. Dinh, S. Han, V. Yaghoobi, H. Xiang, H. Erdelyi, T. Craeghs, J. Segers, W. Van Paepegem, Modeling detrimental effects of high surface roughness on the fatigue behavior of additively manufactured Ti-6Al-4V alloys, *Int. J. Fatigue* (2021), <https://doi.org/10.1016/j.ijfatigue.2020.106034>.
- [46] M. Hamidi Nasab, S. Romano, D. Gastaldi, S. Beretta, M. Vedani, Combined effect of surface anomalies and volumetric defects on fatigue assessment of AlSi7Mg fabricated via laser powder bed fusion, *Addit. Manuf.* 34 (2020), <https://doi.org/10.1016/j.addma.2019.100918>.
- [47] E. Maleki, O. Unal, K. Reza Kashyzadeh, S. Bagherifard, M. Guagliano, A systematic study on the effects of shot peening on a mild carbon steel: microstructure, mechanical properties, and axial fatigue strength of smooth and notched specimens, *Appl. Surf. Sci. Adv.* 4 (2021), <https://doi.org/10.1016/j.apsadv.2021.100071>.
- [48] S. Afkhami, K. Lipiäinen, V. Javaheri, M. Amraei, A. Salminen, T. Björk, Effects of notch-load-defect interactions on the local stress-strain fields and strain hardening of additively manufactured 18Ni300 steel, *Mater. Sci. Eng. A* (2023), <https://doi.org/10.1016/j.msea.2023.145165>.
- [49] K. Solberg, F. Berto, The effect of defects and notches in quasi-static and fatigue loading of Inconel 718 specimens produced by selective laser melting, *Int. J. Fatigue* 137 (2020), <https://doi.org/10.1016/j.ijfatigue.2020.105637>.